AFRL-ML-WP-TP-2006-484

THE EFFECT OF STRAIN-PATH REVERSAL ON CAVITATION DURING HOT TORSION OF Ti-6A1-4V (PREPRINT)

P.D. Nicolaou
S.L. Semiatin

SEPTEMBER 2006

STINFO COPY

MATERIALS AND MANUFACTURING DIRECTORATE
AIR FORCE RESEARCH LABORATORY
AIR FORCE MATERIEL COMMAND
WRIGHT-PATTERSON AIR FORCE BASE, OH 45433-7750

REPORT DOCUMENTATION PAGE

1. REPORT DATE *(DD-MM-YY)*	2. REPORT TYPE	3. DATES COVERED *(From - To)*
September 2006	Journal Article Preprint	N/A

4. TITLE AND SUBTITLE

THE EFFECT OF STRAIN-PATH REVERSAL ON CAVITATION DURING HOT TORSION OF Ti-6A1-4V (PREPRINT)

5a. CONTRACT NUMBER
In-house

5b. GRANT NUMBER

5c. PROGRAM ELEMENT NUMBER
62102F

6. AUTHOR(S)

P.D. Nicolaou (UES, Inc.)
S.L. Semiatin (AFRL/MLLMP)

5d. PROJECT NUMBER
4347

5e. TASK NUMBER
25

5f. WORK UNIT NUMBER
02

7. PERFORMING ORGANIZATION NAME(S) AND ADDRESS(ES)

UES, Inc.
4401 Dayton-Xenia Rd.
Dayton, OH 45432-1894

Processing Section, Metals Branch (AFRL/MLLMP)
Metals, Ceramics, and Nondestructive Evaluation Division
Materials and Manufacturing Directorate
Air Force Research Laboratory, Air Force Materiel Command
Wright-Patterson Air Force Base, OH 45433-7750

8. PERFORMING ORGANIZATION REPORT NUMBER
AFRL-ML-WP-TP-2006-484

9. SPONSORING/MONITORING AGENCY NAME(S) AND ADDRESS(ES)

Materials and Manufacturing Directorate
Air Force Research Laboratory
Air Force Materiel Command
Wright-Patterson AFB, OH 45433-7750

10. SPONSORING/MONITORING AGENCY ACRONYM(S)
AFRL-ML-WP

11. SPONSORING/MONITORING AGENCY REPORT NUMBER(S)
AFRL-ML-WP-TP-2006-484

12. DISTRIBUTION/AVAILABILITY STATEMENT
Approved for public release; distribution is unlimited.

13. SUPPLEMENTARY NOTES
This work has been submitted to ASM International for publication in Metallurgical and Materials Transactions. One or more of the authors is a U.S. Government employee working within the scope of their Government job; therefore, the U.S. Government is joint owner of the work. If published, ASM International may assert copyright. The Government has the right to copy, distribute, and use the work. All other rights are reserved by the copyright owner.
PAO Case Number: AFRL/WS 06-0867, 06 Apr 2006.

14. ABSTRACT

The effect of strain-path reversal on cavitation behavior during the hot torsion testing of an alpha/beta titanium alloy, Ti6AI-4V, with a colony-alpha microstructure was established. Optical microscopy was used to measure cavitation parameters such as cavity size, density, and area fraction. It was observed that when the torsion direction is reversed, the cavitation process is reversed as well; i.e., cavity shrinkage takes place. The experimental observations were interpreted in the context of previous models developed for the densification of porous bodies. For this purpose, the models were modified to treat the effect of colony orientation on the local stress state and the accommodation of the externally-imposed strain, both of which affect the rate of densification/cavity shrinkage. A modified version of the AFRL PM-consolidation model was shown to provide reasonable estimates of the shrinkage kinetics. An alternate description of cavity shrinkage during reversed torsion, analogous to prior descriptions of cavity *growth*, was also developed. It was concluded that the absolute magnitude of the cavity shrinkage rate is smaller than its counterpart during growth because the local stress ratio is lower during reversed straining compared to that during forward straining.

15. SUBJECT TERMS cavitation, reversed torsion, cavity shrinkage, strain-path effects, titanium alloys

16. SECURITY CLASSIFICATION OF:

a. REPORT	b. ABSTRACT	c. THIS PAGE
Unclassified	Unclassified	Unclassified

17. LIMITATION OF ABSTRACT:
SAR

18. NUMBER OF PAGES
42

19a. NAME OF RESPONSIBLE PERSON (Monitor)
David W. Mahaffey

19b. TELEPHONE NUMBER *(Include Area Code)*
N/A

i

THE EFFECT OF STRAIN-PATH REVERSAL ON CAVITATION DURING HOT TORSION OF Ti-6Al-4V

P. D. Nicolaou* and S.L. Semiatin

Air Force Research Laboratory, Materials and Manufacturing Directorate,

AFRL/MLLM, Wright-Patterson Air Force Base, OH 45433-7817, USA

*El. Venizelou 31, 191 00, Megara, GREECE

Tel. +30-229-602 5492, Fax, +30-229-602 5492, e-mail: NicolaouP@aget.gr

Abstract

The effect of strain-path reversal on cavitation behavior during the hot torsion testing of an alpha/beta titanium alloy, Ti-6Al-4V, with a colony-alpha microstructure was established. Optical microscopy was used to measure cavitation parameters such as cavity size, density, and area fraction. It was observed that when the torsion direction is reversed, the cavitation process is reversed as well; i.e., cavity shrinkage takes place. The experimental observations were interpreted in the context of previous models developed for the densification of porous bodies. For this purpose, the models were modified to treat the effect of colony orientation on the local stress state and the accommodation of the externally-imposed strain, both of which affect the rate of densification/cavity shrinkage. A modified version of the AFRL PM-consolidation model was shown to provide reasonable estimates of the shrinkage kinetics. An alternate description of cavity shrinkage during reversed torsion, analogous to prior descriptions of cavity *growth*, was also developed. It was concluded that the absolute magnitude of the cavity shrinkage rate is smaller than its counterpart during growth because the local stress ratio is lower during reversed straining compared to that during forward straining.

I. INTRODUCTION

The bulk hot working of engineering alpha/beta titanium alloys such as Ti-6Al-4V is commonly used to convert coarse grain, colony-alpha ingot microstructures into fine, equiaxed-alpha billet structures. Despite the apparent simplicity of the processes employed (e.g. open-die forging, cogging, upsetting), relatively complex states of stress and strain are typically generated within the workpiece; the complexity of industrial operations is also increased due to changes in strain path. Furthermore, processing may give rise to undesirable defects in finished wrought products. These defects include gross fracture, shear bands, and internal cavities. The initiation and growth of internal cavities is particularly important because such deleterious defects may eventually lead to gross fracture during subsequent manufacturing steps or in service [1-3].

A considerable amount of research has been devoted to developing an understanding of cavitation behavior for a wide range of metals and alloys [4-6]. Most of these efforts have focused on the determination of the conditions under which cavitation can be fully suppressed (or at least minimized) or quantifying cavity-growth kinetics as a function of a stress state [7-9]. In the majority of early research on cavitation kinetics, the stress ratio (i.e., the ratio of hydrostatic-to-effective stress) was usually equal to or greater than that corresponding to uniaxial tension, viz., 1/3. By contrast, Bae et al. [10] and Nicolaou et al. [11] have recently investigated cavitation under a macroscopic state of stress consisting of simple shear. For example, Nicolaou, et al. used hot torsion testing to establish the effect of shear deformation on the cavitation behavior of the alpha/beta titanium alloy Ti-6Al-4V with a colony-alpha microstructure over a wide range of strains. Local texture and thus the non-uniform deformation associated with adjacent hard and soft colony

2

orientations were taken into account in the analysis. The results were compared to other findings for the uniaxial- and notched- tension testing of Ti-6Al-4V with an identical (colony-alpha) microstructure [7, 12].

The present work is a continuation of earlier efforts on cavitation during monotonic torsion testing. The specific objective of this research was to establish and model the effect of *strain-path reversal* on the cavitation behavior of the Ti-6Al-4V alloy. To this end, hot torsion tests comprising forward and reversed straining were conducted. The cavitation in deformed specimens was characterized using optical and scanning-electron microscopy. The experimental measurements were interpreted in the context of several different modeling approaches.

II. MATERIALS AND PROCEDURES

Hot torsion tests comprising forward and reversed straining were conducted on Ti-6Al-4V to establish cavitation behavior for a prototypical, non-monotonic strain path. The Ti-6Al-4V alloy used in this work was the same as in previous monotonic torsion tests [11], and hence will be described only briefly. As before, the material was beta annealed to produce relatively fine beta grains with a mixed colony, basketweave microstructure. The beta grain size (and comparable colony size) was ~100 μm; the heat treatment also produced a grain-boundary alpha layer approximately 3 μm thick. The material had a weak texture; the principal texture components comprised one with the c-axis parallel to the bar axis having an intensity of ~2.2 x random and another characterized by the c-axis tilted ~60° from the bar axis with approximately 1.5 x random intensity.

The torsion specimen geometry was the same as in the monotonic tests [11]. All tests were conducted under isothermal conditions at a temperature of 815°C using

3

a constant forward/reverse twist rate of 4.8°/s, which corresponded to a surface von Mises effective strain rate of 0.04 s^{-1}. Following a 10-minute soak at temperature, each test specimen was deformed in the forward mode to a twist angle between 90° and 250° in order to impose different amounts of strain. The twisting direction was then reversed quickly (the "dwell" time for the change of twisting direction was ~1-2 seconds), and torsion to a reverse twist angle between 30° and 250° degrees was imposed followed by water quenching of the sample.

The torque-twist data were converted to effective stress-effective strain using standard equations [11].

After testing, *axial-tangential* cross sections near the outer surface of the specimen containing the z-θ plane were prepared for metallographic examination. The cavity size and shape were measured on as-polished specimens using optical micrographs taken at a magnification of 200X and the image-analysis software ImageJ Version 1.32. Specifically, scanned micrographs were transformed into pure black and white pictures, from which the cavities could be clearly distinguished from the fully dense matrix. The Image software was then used to determine the area of each individual cavity. Higher-magnification backscattered-electron images were also taken in a Leicascan™ 360FE scanning-electron microscope in order to obtain a more detailed picture of the microstructure.

III. MODELING PROCEDURES

The local stresses and strains developed in regions containing hard and soft colonies were estimated and used in models of pore closure in order to interpret cavity shrinkage during reversed-torsion testing.

A. *Local Stress State*

A representative volume element (comprising a hard colony, a soft colony, and a hard colony), similar to the one used earlier for the analysis of cavitation during uniaxial tension testing [12], was utilized in the present work in order to determine the magnitude of the stresses and strains developed locally as a result of the different deformations that adjacent hard and soft colonies undergo. As in the case of uniaxial tension, the soft colonies were of prime interest because they accumulate most of the externally imposed strain and hence are the ones that govern the cavitation behavior of the material.

In contrast to uniaxial tension, in which the axis of the representative volume element (RVE) was assumed to coincide with the loading direction of the specimen [12], the angle λ between the RVE axis and the torsion/sample axis was allowed to vary (Figure 1). Because of the simple-shear nature of the externally applied stress (Figure 1), the macroscopic normal stresses (σ_z^{mac} and σ_θ^{mac}) in the torsion-sample axis system (r-z-θ) are zero, while the shear stress $\tau_{z\theta}^{mac}$ has a finite value equal to $\dfrac{\overline{\sigma}^{mac}}{\sqrt{3}}$, in which $\overline{\sigma}^{mac}$ is the flow stress of the RVE. For a non-zero value of the angle λ (Figure 1), the transformation of the stress tensor from the z-θ axes to the z'-θ' axes gives rise to the following equations for the macroscopic stresses:

$$\sigma_{\theta'}^{mac} = -2\frac{\overline{\sigma}^{mac}}{\sqrt{3}}\ \sin\lambda\ \cos\lambda, \tag{1a}$$

$$\sigma_{z'}^{mac} = 2\frac{\overline{\sigma}^{mac}}{\sqrt{3}}\ \sin\lambda\ \cos\lambda \tag{1b}$$

$$\tau_{z'\theta'}^{mac} = \frac{\overline{\sigma}^{mac}}{\sqrt{3}}\ \left(\cos^2\lambda\ -\sin^2\lambda\right) \tag{1c}$$

Note that for $\lambda = 0$, the stresses from Equation (1) reduce to those in the z-θ coordinate system, i.e.,

$$\tau_{z'\theta'}{}^{mac} = \frac{\overline{\sigma}^{mac}}{\sqrt{3}}, \; \sigma_{z'}^{mac} = \sigma_z^{mac} = 0, \text{ and } \sigma_{\theta'}^{mac} = \sigma_\theta^{mac} = 0,$$

while for $\lambda = 45^o$,

$$\sigma_{z'}^{mac} = \frac{\overline{\sigma}^{mac}}{\sqrt{3}}, \; \sigma_{\theta'}^{mac} = -\frac{\overline{\sigma}^{mac}}{\sqrt{3}}, \text{ and } \tau_{z'\theta'}{}^{mac} = 0.$$

The local stress state within the soft and the hard colonies was determined using the equilibrium equations and yield functions for the two types of colonies. The overall analysis was conducted in a manner similar to that described in Reference 13, describing cavitation behaviour under complex stress states as in open-die forging.

1. Equilibrium Equations

For the macroscopic state of simple shear imposed during torsion, it was assumed that $\sigma_{r'}{}^{mac} = \sigma_{r'_h} = \sigma_{r'_s} \approx 0$. Furthermore, $\tau_{z'r'_s} = \tau_{\theta'r'_s} = \tau_{z'r'_h} = \tau_{\theta'r'_h} \approx 0$, in which the subscripts z', θ' and r' refer to the specific stress component in the rotated coordinate system.

In deriving the equilibrium equations, the stresses $\sigma_{\theta'}{}^{mac}$ and $\tau_{z'\theta'}{}^{mac}$ were each assumed to be a rules-of-mixture average of the corresponding stress components in the hard and soft colonies, i.e.,

$$\sigma_{\theta'}^{mac} = f_h \sigma_{\theta'_h} + (1 - f_h) \sigma_{\theta'_s} \tag{2}$$

$$\tau_{z'\theta'}^{mac} = f_h \tau_{z'\theta'_h} + (1 - f_h) \tau_{z'\theta'_s} \tag{3}$$

in which f_h represents the volume fraction of the hard colonies, and the subscripts h and s refer respectively to the hard or soft colonies. Furthermore, it was assumed that

6

$$\sigma_{z'_h} = \sigma_{z'}^{mac} \tag{4a}$$

$$\sigma_{z'_s} = \sigma_{z'}^{mac} \tag{4b}$$

2. Yield Functions

The yield functions for the hard and soft colonies in the rotated coordinate system may be written as:

$$\bar{\sigma}_h = \frac{1}{\sqrt{2}}\left\{\left(\sigma_{z'_h} - \sigma_{\theta'_h}\right)^2 + \left(\sigma_{z'_h}\right)^2 + \left(\sigma_{\theta'_h}\right)^2 + 6\tau_{z'\theta'_h}^2\right\}^{1/2} \tag{5}$$

$$\bar{\sigma}_s = \frac{1}{\sqrt{2}}\left\{\left(\sigma_{z'_s} - \sigma_{\theta's}\right)^2 + \left(\sigma_{z'_s}\right)^2 + \left(\sigma_{\theta's}\right)^2 + 6\tau_{z'\theta's}^2\right\}^{1/2} \tag{6}$$

$\bar{\sigma}_s$, $\bar{\sigma}_h$ denote the flow stress of the soft and hard colonies, respectively.

The flow stresses of the soft and hard colonies, $\bar{\sigma}_s$ and $\bar{\sigma}_h$, are related to the overall RVE flow stress by applying the self-consistent hypothesis [14], i.e.,

$$\bar{\sigma}^{mac} = f_h\bar{\sigma}_h + \left(1 - f_h\right)\bar{\sigma}_s \tag{7}$$

The above equation can be rewritten as:

$$\bar{\sigma}^{mac} = f_h k_h\left(\dot{\bar{\varepsilon}}_h\right)^m\left(\bar{\varepsilon}_h\right)^n + \left(1 - f_h\right)k_s\left(\dot{\bar{\varepsilon}}_s\right)^m\left(\bar{\varepsilon}_s\right)^n \tag{8}$$

in which k_h, k_s are the strength coefficients of the hard/soft colonies, which are assumed to depend only on the Taylor factors M_h and M_s; $\bar{\varepsilon}$, $\dot{\bar{\varepsilon}}$ denote the effective strain and strain rate, respectively; and m and n are the strain rate sensitivity index and the strain exponent.

3. Solution of the System of Equations

Using the self-consistent model [14] and Equations (7) and (8), the values of the flow stresses in the hard $(\bar{\sigma}_h)$ and soft $(\bar{\sigma}_s)$ colonies can be determined for specific values of f_h as well as k_h and k_s, which depend only on the Taylor factors. The macroscopic flow stress is an experimental measurement.

Using Equations (1) and the measured value of $\bar{\sigma}^{mac}$, the stresses $\sigma_{z'}^{mac}$, $\sigma_{\theta'}^{mac}$, and $\tau_{z'\theta'}^{mac}$ are calculated for a given angle λ. From Equations (2), (3), (4a), (4b), (5), and (6), the six unknowns $\sigma_{z'_h}$, $\sigma_{\theta'_h}$, $\sigma_{z'_s}$, $\sigma_{\theta'_s}$, $\tau_{z'\theta'_h}$, $\tau_{z'\theta'_s}$ are then determined.

B. *Cavity-Closure Models*

As will be described in Section IV, the cavity fraction decreased during reversed straining in torsion. To describe the rate of cavity shrinkage, therefore, two previously-developed models for pore closure during powder consolidation were employed. The first approach was developed by Dutton, et al. [15] and the second by Liu, et al. [16]. The basic features of each model are summarized in this section.

1. Dutton, et al. (AFRL) Model

This model was developed at the Air Force Research Laboratory (AFRL) by Dutton, et al. [15] and applied later by DeLo et al. [17]. It is a hybrid continuum-micromechanical model. That is to say, it combines (1) continuum aspects relating macroscopic strain rates and macroscopic (deviatoric and hydrostatic) stresses and (2) micromechanical aspects such as the effect of pore geometry and deformation mechanism on densification. The model enables the detailed description of an arbitrary mode of deformation based on measurements from relatively simple, calibration modes of deformation such as uniaxial compression [17].

The AFRL model deals with a rate-sensitive, plastically deforming material. The macroscopic strain rates of the porous body are calculated from the following expression:

$$\dot{\varepsilon}_{ij} = \left(\frac{K(D)\phi^2 \dot{\bar{\varepsilon}}}{\bar{\sigma}} \right) \left[(1+\nu)\sigma'_{ij} + (1-2\nu)\sigma_m \delta_{ij} \right] \tag{9}$$

8

in which $\dot{\varepsilon}_{ij}$ denotes the macroscopic strain rate, σ'_{ij} is the deviatoric stress, σ_m the mean stress, $\bar{\sigma}$ is the effective stress, ν is the Poisson's ratio of the porous body; and ϕ is the stress intensification factor. The term K(D) is associated with the relative density D; it is commonly assumed to be equal to D.

The flow behavior of the *fully dense compact*, is assumed to be:

$$\bar{\sigma} = B\dot{\bar{\varepsilon}}^m \, , \tag{10}$$

in which m is the strain rate sensitivity index and B the temperature-dependent strength factor.

There have been a number of efforts to correlate the stress intensification factor ϕ to the relative density of a porous body [18, 19]. In the present work, the simple relationship derived by Coble [20] (i.e., $\phi = 1/D$) was used. This is because the densities in the current work were well above 95%, and the Coble relationship describes experimental observations very well at such levels of porosity.

From Equation (9), the strain-rate components can be determined for any state of stress. The densification rate $\dot{D}$ is then obtained as the sum of the principal strain-rate components, i.e.,

$$\dot{D} = -\left(\dot{\varepsilon}_{11} + \dot{\varepsilon}_{22} + \dot{\varepsilon}_{33}\right) \tag{11}$$

2. Liu, et al. Model

The second model used in the interpretation of the experimental results was originally developed by Liu, Wadley, and Duva [16]. In this formulation, the strain rates developed in a porous body subjected to a multiaxial state of stress is described by the relation:

$$\dot{\varepsilon}_{ij} = AS^{N-1}\left(\frac{3a}{2}\sigma'_{ij} + \frac{b}{3}\sigma_m\delta_{ij}\right). \tag{12}$$

in which N is the stress exponent (= 1/m), A is a temperature-dependent constant (defined from the constitutive behavior of the fully dense compact, $A = \dot{\bar{\varepsilon}}/\bar{\sigma}^N$), and the term S is defined as:

$$S^2 = a\bar{\sigma}^2 + b\sigma_m^2 \tag{13}$$

The parameters a and b are related to the relative density. According to Duva and Crow [21], they are given by the following equations:

$$a = \frac{1 + \frac{2}{3}(1-D)}{D^{2N/(N+1)}} \quad \text{and} \quad b = \left[\frac{N(1-D)}{\left(1 - (1-D)^{1/N}\right)^N}\right]^{2/n+1} \left(\frac{3}{2N}\right)^2 \tag{14}$$

As for the AFRL model, the cavity-shrinkage rate from the Liu, et al. model was obtained as the sum of the principal strain-rate components (Equation (11)) determined from Equation (12).

IV. RESULTS AND DISCUSSION

The principal results of this work included measurements of the flow behavior and cavitation during reversed torsion, model predictions of cavity shrinkage, and interpretation of cavity growth during forward straining versus cavity shrinkage during reversed straining.

A. *Flow Behavior*

Sample effective stress-effective strain curves for four different torsion tests are presented in Figure 2. For these tests, the deformation path comprised a forward strain of 0.99 or 1.78 followed by a reverse strain between 0.50 and 1.78. During the forward deformation, the peak stress was achieved at a strain of ~0.06. This peak was followed by extensive flow softening; the softening exponent[*] n was found to be approximately -0.20, which is consistent with previous measurements in compression

---

[*] The strain exponent is defined by the following equation: $\bar{\sigma} = K\bar{\varepsilon}^n$.

of a similar material [22], as well as those from monotonic torsion tests [11]. After reversing the strain path, strain hardening occurred until a peak stress was achieved at a strain increment of ~0.20 from the beginning of the reversed loading. However, in contrast to the behavior during the initial (forward) loading, subsequent flow softening was absent; i.e., the exponent n was less than 0.02. The observed flow behavior (Figure 2) resembles that found by Poths, et al. [23, 24] during torsion testing of a similar material but at a somewhat different strain rate. The explanation for the reloading transients in reversed torsion tests may lie in the nature of the microscopic slip process. Specifically, the initial flow softening (at low strains) is due to slip transfer across the alpha-beta interfaces. When the deformation is reversed, there may be a large number of mobile dislocations which can move easily in the reverse direction. Because the original alpha-beta interfaces have now been broached, it may be easier to form subgrain-like substructures in both the alpha and beta phases, thus leading to near steady-state flow.

B. *Metallographic Observations*

Optical micrographs illustrating cavitation observations are shown in Figure 3. The micrographs were taken at the surface of specimens twisted to a forward effective strain of 0.99 (twist angle of 125°) and reverse strains of 0, 0.25, 0.50, or 1.98. The micrographs show that the cavity area fraction developed during forward straining was small, and it decreased with increasing reversed deformation. On the other hand, there were no noticeable differences with regard to the cavity shape, which is mainly elliptical, similar to what was found previously in monotonic torsion tests [11].

The fraction of cavities within a specific size range for three different testing conditions (i.e., a forward strain of 0.99 and reverse strains of 0, 0.50, or 0.99) is shown in Figure 4. These results revealed that the fraction of the larger cavities

decreased as the reverse strain increased, implying that cavity shrinkage occurred during reverse torsion.

A range of angles λ between the z-axis of the specimen and the axis of the RVE was noted in micrographs of polished and etched specimens (e.g., Figure 5 for a specimen for which $\bar{\varepsilon}_{forward}$ =0.99 and $\bar{\varepsilon}_{reverse}$ = 1.98). The dashed lines, which outline hard colonies (established via EBSD [11]), aid in the visualization of the angles in Figure 5.

C. *Cavity Density*

Metallographic observations for different test conditions (Figure 6) revealed that the cavity density (i.e., number of cavities per mm^2) did not show any essential variation with increasing strain. In addition, the results indicated that the number density of cavities was smaller by a factor of ~2-3 times compared to the cavity densities developed in the same material during uniaxial tension [12]. Two factors may explain this trend. First, the cavity *nucleation* rate is probably lower is torsion inasmuch as the maximum principal (normal) stress in simple shear is lower compared to that during uniaxial tension. Second, the cavity-*growth* rate is smaller in shear than in uniaxial tension. Thus, there is likely a large number of small cavities which cannot be distinguished at the magnification (200X) at which cavitation was examined. These small cavities, however, can be imaged in high-magnification SEM micrographs (e.g., Figure 7).

D. *Stress Ratios*

Calculations of the ratio of the mean σ_m to effective stress $\bar{\sigma}$ (i.e., the stress ratio) in the soft colony as a function of the angle λ are shown in Figure 8. The stress ratio was calculated for two different ratios of the Taylor factors of the hard and the soft colonies (i.e., M_h/M_s = 2 or 3). Although the reverse stage of straining is of

12

prime interest, the variation of the stress ratio during the first (forward) stage is also shown in Figure 8 for comparison. During the forward strain, $\sigma_m/\bar{\sigma}$ is positive. When the loading direction is reversed the stress ratio becomes negative because the sign of the principal stresses is reversed. Therefore, cavity shrinkage instead of growth is promoted. Because the overall macroscopic stress state is simple shear, the stress ratio is zero for $\lambda = 0°$. As λ increases toward 45°, $\sigma_m/\bar{\sigma}$ also increases, reaching its maximum value at $\lambda = 45°$.

From the self-consistent model, the flow stress of the soft colonies was estimated to be 113 MPa and 94.5 MPa for M_h/M_s equal to 2 or 3, respectively. The ratio of the normal stress ($\sigma_z^{'}$ or $\sigma_\theta^{'}$) to the effective stress developed in the soft colonies during the reverse stage of torsion as a function of λ and $M_h/M_s = 2$ or 3 is shown in Figure 9. The results indicate that the magnitude of the normal stresses increases as λ increases and that the ratios are higher when M_h/M_s increases.

E. *Model Predictions of Cavity Shrinkage*

Predictions of the AFRL and the Liu, et al. pore-closure models are presented in Figure 10 in terms of the cavity fraction as a function of effective strain $\bar{\varepsilon}$ for a ratio of the Taylor factors (of the hard and soft phases) equal to 2, an initial cavity fraction of 2.1 pct., and values of λ of 15°, 25°, and 45°. Because of the non-softening flow behavior during reversed torsion, the constitutive behavior was taken to be $\bar{\sigma} = 230 \ \dot{\bar{\varepsilon}}^{0.15}$, or $\dot{\bar{\varepsilon}} = 1.8x10^{-16} \ \bar{\sigma}^{6.67}$. A comparison of the different model results reveals that the Liu, et al. approach predicts higher densification rates compared to the AFRL model. Furthermore, the results mirror the dependence of the stress ratio on λ (Figures 8 and 9) inasmuch as the predicted densification rate is small when λ is small, but increases significantly when λ approaches 45°.

F. *Comparison of Model Predictions with Experimental Results*

Measurements of the cavity area fraction in the z-θ plane as a function of the effective strain during the reverse stage of deformation were compared to model predictions based on the AFRL and the Liu, et al. approaches (Figure 11). The individual data points correspond to experimental measurements for initial (forward) strains of either 0.99 or 1.78 (i.e., twist angles of 125° and 225°, respectively). The results for an effective (reverse) strain of zero are those from the monotonic tests. Overall, the measured evolution of the cavity fraction follows a trend commonly observed during the latter stages of the consolidation process of porous bodies, i.e., there is a continuous reduction in the densification rate with increasing strain/density.

In Figure 11, there are two lines for each model and initial (forward) strain, one for an assumed ratio of the Taylor factors of the hard and soft colonies (M_h/M_s) equal to 2 and one for M_h/M_s equal to 3. Each line is an average of the simulation results for different angles λ from 0 to 45° in steps of 5°. The AFRL model shows better overall agreement with the experimental results compared to the Liu, et al. model, which tends to overestimate the rate of cavity closure, particularly for the results corresponding to the larger forward strain (Figure 11b).

It should be emphasized that the model results in Figure 11 assume no rotation of the microstructure *during* torsion. In reality, microstructure rotation does occur, and the initial angle λ between the z-axis of the specimen and the axis of the RVE changes as well. The magnitude of such change depends on the imposed strain (i.e., the amount of twist), and the resistance imposed from the soft and the hard colonies. If such resistance is ignored and the material is treated as a continuum, the change of angle λ, Δλ, is given by the following equation:

$$\Delta\lambda = \arctan\gamma, \qquad\qquad (15)$$

14

in which γ denotes the shear strain.

The assumption of either zero rotation or free rotation of the microstructure represents the two bounds for the present problem. Figure 12 summarizes the predicted rates of densification using the AFRL model for the two bounds. As in Figure 10, these curves represent the average for an *initial* range of λ between $0°$ and $45°$. The results reveal that a faster densification rate is predicted when microstructure rotation is taken into account. Furthermore, for the lower initial cavitation level (Figure 12a) it is observed that the experimental results are bounded by the two extreme cases. On the other hand, for the higher initial cavitation level (Figure 12b), the experimental results are located in the vicinity of the no-rotation predictions.

G. *Engineering Approach to Cavity Shrinkage*

A phenomenological approach was also developed to quantify the kinetics of cavity shrinkage during reversed torsion. This approach was based on the previous large body of research dealing with cavity *growth* under different deformation conditions. These former efforts established the magnitude of the so-called called cavity growth-rate parameter η in the following relation:

$$C = C_o \exp(\eta \bar{\varepsilon}) \qquad , \qquad (16)$$

in which C and C_o denote the cavity volume or area fraction at an effective strain $\bar{\varepsilon}$ and the initial cavity volume fraction, respectively.

In the present work, the reverse deformation during which cavity shrinkage occurs was of major interest. For cavity shrinkage, the value of η in Equation (16) is negative. Furthermore, the factor C_o in this equation is replaced by $C_{forward}$, the cavity fraction at the end of the forward torsion stage, i.e., a value determined from monotonic tests [11]. A semi-logarithmic plot of $C/C_{forward}$ as a function of effective

15

strain (Figure 13) was prepared to determine the value of η during reverse torsion. The slope of the resulting straight line (= $d\ln(C/C_{forward})/d\varepsilon$) was -0.52; i.e., η = -0.52. In absolute terms, this value of η is lower than the one found in the monotonic (forward) torsion tests, viz., $\eta \approx 0.75$ for the z-θ plane.

The two values of η were interpreted in the context of the deformation that occurs in forward versus reverse torsion. When the strain path is reversed, the stress ratio in the soft colony of the RVE changes sign from positive to negative (Figure 8). At this point, cavity growth ceases and cavity shrinkage commences. However, the rate of cavity shrinkage is not as fast as the previous rate of growth because the absolute value of the stress ratio is higher during growth. This difference in the magnitude of the stress ratios arises from the fact that during the forward motion the material undergoes extensive flow softening, while its flow stress is essentially independent of strain during the second stage. Specifically, during the reverse torsion stage, in which the flow softening rate is zero, the flow stress of the hard and the soft colonies remain constant. On the contrary, during the forward stage, the material undergoes extensive flow softening, which leads to a decrease in the flow stress of both the hard and the soft colonies. However, the flow stress of the soft phase drops at a faster rate because it accumulates a larger portion of the externally imposed strain. Thus, the difference in the flow stress between hard and soft colonies is larger in the forward stage of deformation. Because the secondary stresses and therefore the stress ratio in the soft colonies increase as this difference in the flow stress increases, the stress ratio is lower in the reverse stage. As a result, the absolute value of η is lower during the reverse deformation regime.

16

V. SUMMARY AND CONCLUSIONS

The alpha/beta titanium alloy Ti-6Al-4V with a colony microstructure was deformed in reversed torsion at a temperature of 815°C and surface effective strain rate of 0.04 s^{-1} in order to establish the effect of a strain-path change on deformation and cavitation behavior. Effective stress – effective strain curves revealed extensive flow softening during the forward deformation but minimal softening after the reversal of the torsion direction. Optical microscopy was used to establish damage characteristics in terms of the size, density, and area fraction of cavities developed during both forward and reversed torsion. In order to interpret these results, a model describing the effect of the orientation of adjacent soft and hard colonies on local stresses and strains and hence cavitation behavior was developed. It was found that cavities developed during forward straining shrink when a reverse strain is applied. This finding is consistent with the sign of the stress ratio, which changes from positive during the forward strain to negative upon reversal. The experimental observations were compared to two prior models which describe the densification of porous bodies. The comparison of the measurements to the model predictions revealed that the AFRL model provides better agreement with the experimental findings. In addition, the specific rate at which cavities shrink during the reverse stage of the torsion testing was determined from plots of the cavity area fraction as a function of effective strain. It was concluded that the absolute magnitude of the cavity-shrinkage rate is smaller than its counterpart during growth because the local stress ratio is lower during reversed straining.

REFERENCES

1. S.L. Semiatin: in *Handbook of Workability and Process Design*, G.E. Dieter, H.A. Kuhn, and S.L. Semiatin, eds., ASM International, Materials Park, OH, 2003, Chapter 13.

2. S.L. Semiatin, R.L. Goetz, E.B. Shell, V. Seetharaman, and A.K. Ghosh: *Metall. Mater. Trans. A*, 1999, vol. 30A, pp. 1411-1424.

3. J.C. Williams and E.A. Starke, Jr.: in *Deformation, Processing, and Structure*, ASM, Metals Park, OH, 1982, Chapter 7.

4. B.P. Kashyap and M.K. Mukherjee: *Res Mechanica*, 1986, vol. 17, pp. 293-355.

5. A.H. Chokshi: *J. Mater. Sci.*, 1986, vol. 21, pp. 2073-2080.

6. R. Verma, P.A. Friedman, A.K. Ghosh, S. Kim, and C. Kim: *Metall. Mater. Trans. A*, 1996, vol. 27A, pp. 1889-1898.

7. P.D. Nicolaou, R.L. Goetz, and S.L. Semiatin: *Metall. Mater. Trans. A*, 2004, vol. 35A, pp. 655-663.

8. H. Agarwal, A.M. Gokhale, S. Graham, and M.F. Horstemeyer: *Mater. Sci. Eng. A*, 2003, vol. A341, pp. 35-42.

9. J. Pilling and N. Ridley: *Acta Metall.*, 1986, vol. 34, pp. 669-679.

10. D.H. Bae, A.K. Ghosh, and J.R. Bradley: *Metall. Mater. Trans. A*, 2003, vol. 34A, pp. 2449-2463.

11. P.D. Nicolaou, J.D. Miller, and S.L. Semiatin: *Metall. Mater. Trans. A*, 2005, vol. 36A, pp. 3461-3469.

12. T.R. Bieler, P.D. Nicolaou, and S.L. Semiatin: *Metall. Mater. Trans. A*, 2005, vol. 36A, pp. 129-140.

13. P.D. Nicolaou and S.L. Semiatin: *Metall. Mater. Trans. A*, 2005, vol. 36A, pp. 1567-1574.

14. S.L. Semiatin, F. Montheillet, G. Shen, and J.J. Jonas: *Metall. Mater. Trans. A*, 2002, vol. 33A, pp. 2719-2727.

15. R.E. Dutton, S. Shamasundar, and S.L. Semiatin: *Metall. Mater. Trans. A*, 1995, vol. 26A, pp. 2041-2052.

16. Y.-M. Liu, H.N.G. Wadley, and J.M. Duva: *Acta Metall. Mater.*, 1994, vol. 42, pp. 2247-2260.

17. D.P. DeLo, R.E. Dutton, S.L. Semiatin, and H.R. Piehler: *Acta Mater.*, 1999, vol. 47, pp. 3159-3167.

18. S. Shamasundar, R.E. Dutton, and S.L. Semiatin: *Scripta Metall. Mater.*, 1994, vol. 31, pp. 521-525.

19. A.S. Helle, K.E. Easterling, and M.F. Ashby: *Acta Metall.*, 1985, vol. 33, pp. 2163-2174.

20. R.L. Coble: *J. Appl. Phys.*, 1961, vol. 32, pp. 787-792.

21. J.M. Duva and Crow: *Acta Metall. Mater.*, 1992, vol. 49, pp. 31-40.

22. R.M. Miller, T.R. Bieler, and S.L. Semiatin: *Scripta Mater.*, 1999, vol. 40, pp. 1387-1393.

23. R.M. Poths, G. Angella, B.P. Wynne, W.M. Rainforth, S.L. Semiatin, and J.H. Beynon: *Metall. Mater. Trans. A*, 2004, vol. 35A, pp. 2993-3001.

24. R.M. Poths, B.P. Wynne, W.M. Rainforth, S.L. Semiatin, and J.H. Beynon: in *Ti-2003: Science and Technology*, G. Luetjering and J. Albrecht, eds., Wiley-VCH Verlag GmbH, Weinheim, Germany, 2004, pp. 1243-1250.

Figure Captions

Figure 1. Representative volume element (comprising hard-soft-hard colonies) lying at an angle λ relative to the axial direction (z) of the specimen.

Figure 2. Effective stress-strain curves for Ti-6Al-4V deformed in torsion at 815°C and a surface effective strain rate of 0.04 s^{-1}. The forward and reverse effective strains are indicated on each curve.

Figure 3. Optical micrographs from as-polished specimens which were tested in reversed torsion. For all micrographs, the forward (surface) effective strain was 0.99, while the reverse (surface) effective strain was (a) 0, (b) 0.25, (c) 0.50, or (d) 1.98.

Figure 4. Fraction of cavities within a specific size range for three different deformation conditions. In all cases, the forward (surface) effective strain was 0.99.

Figure 5. Optical micrograph showing the angle λ between the z-axis of the specimen and the axis of an RVE for a torsion test for which $\bar{\varepsilon}$ forward $= 0.99$ and $\bar{\varepsilon}$ reverse $= 1.98$

Figure 6. Cavity density as a function of (surface) effective strain during reversed torsion for two different levels of applied forward strain.

Figure 7. Backscattered-electron SEM micrograph showing the presence of small cavities for a torsion test for which $\bar{\varepsilon}$ forward $= 0.99$, and $\bar{\varepsilon}$ reverse $= 0.50$.

Figure 8. Variation of the stress ratio $\sigma_m/\bar{\sigma}$ with the angle λ during the forward and reversed stages of torsion testing.

Figure 9. Dependence of the ratio of the normal-to-effective stress with λ during the reversed stage of torsion testing. The flow stress of the soft colonies was estimated to be 113 MPa and 94.5 MPa for M_h/M_s of 2 or 3, respectively.

Figure 10. Cavity-closure predictions as a function of the reverse effective strain and the angle λ based on either the AFRL model or the Liu, et al model.

Figure 11. Comparison of model predictions and experimental measurements of the variation of cavity fraction with (reverse) effective strain for two different levels of initial cavity fraction: (a) 1% and (b) 2.1%. The predictions of the AFRL and the Liu, et al. models are plotted for two different ratios of the Taylor factor between the hard and the soft phase, M_h/M_s. The model predictions represent an average for λ between 0 and 45°.

Figure 12. Effect of microstructure rotation on the predictions of the AFRL model, for two different ratios of the Taylor factor between the hard and the soft phase, M_h/M_s and for two different levels of initial cavity fraction: (a) 1% and (b) 2.1%. The model predictions represent an average for λ between 0 and 45°. The experimental measurements are also shown in the graph.

Figure 13. Semi-logarithmic plot of the ratio of the cavity fraction at a reverse strain $\bar{\varepsilon}$ to the cavity fraction at the beginning of strain path reversal as a function of the reverse strain.
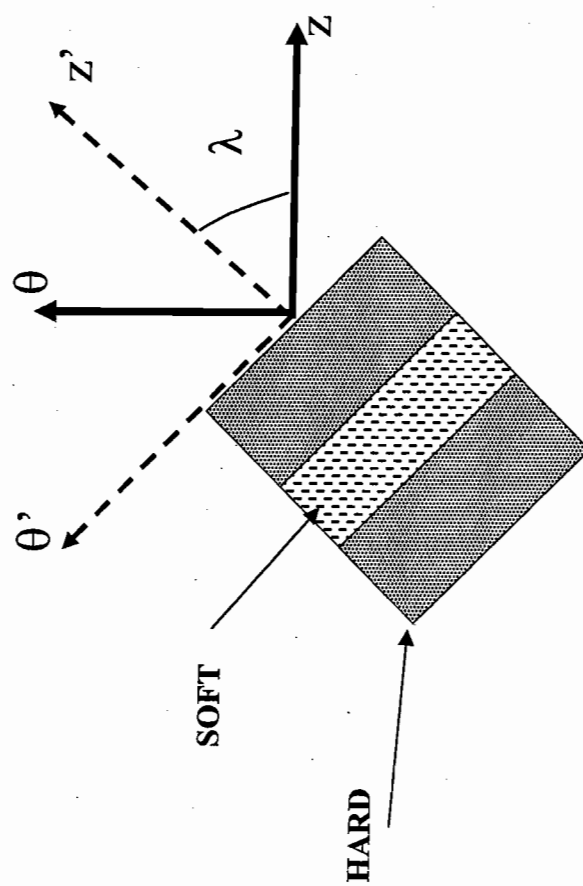
FIGURE 1

FIGURE 2

23

FIGURE 3

FIGURE 4

25

λ= 0°

λ= 18°

λ= 25°

100 μm

λ= 27°

λ= 19°

λ= 42°

N

θ

FIGURE 5

26
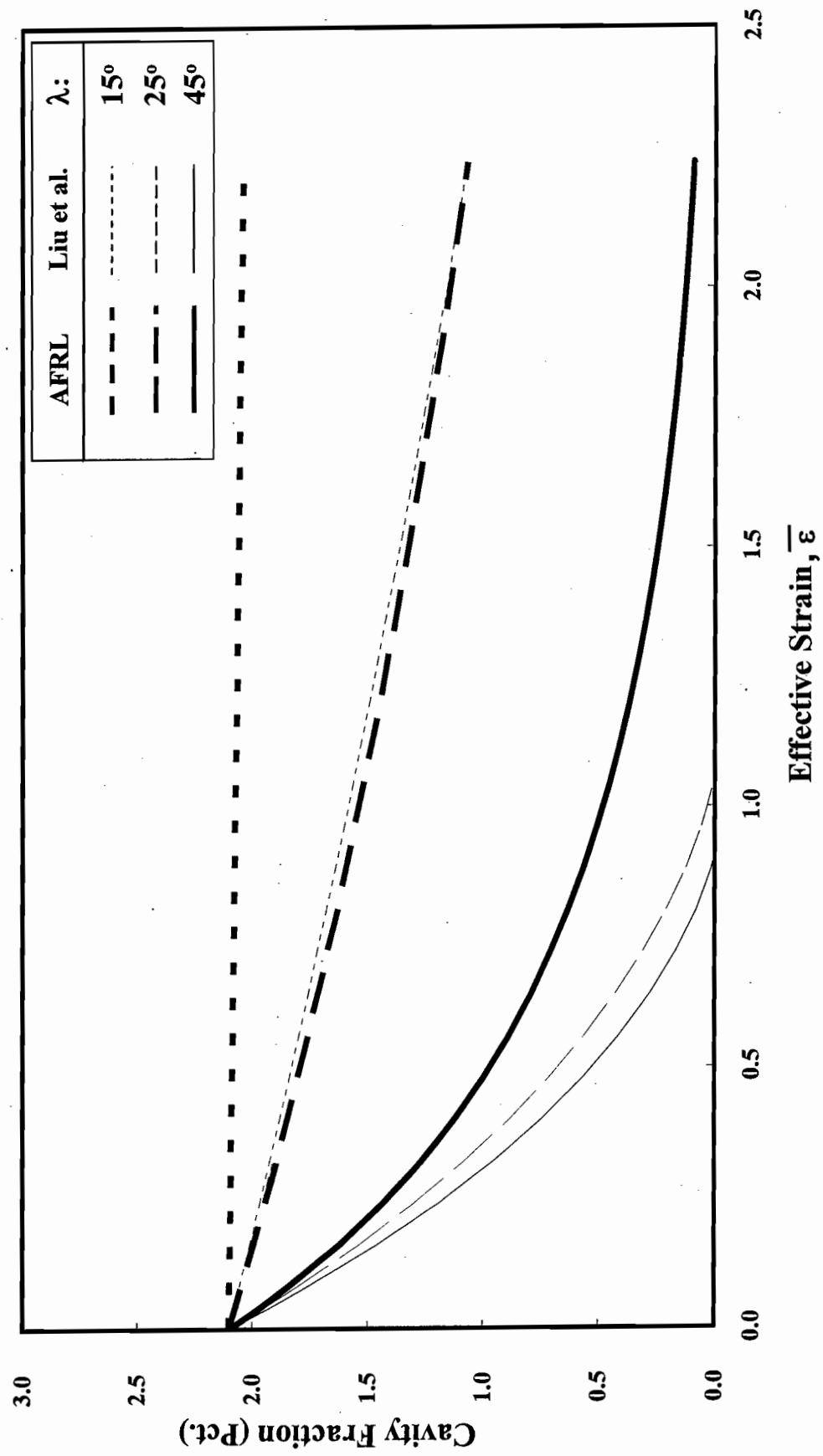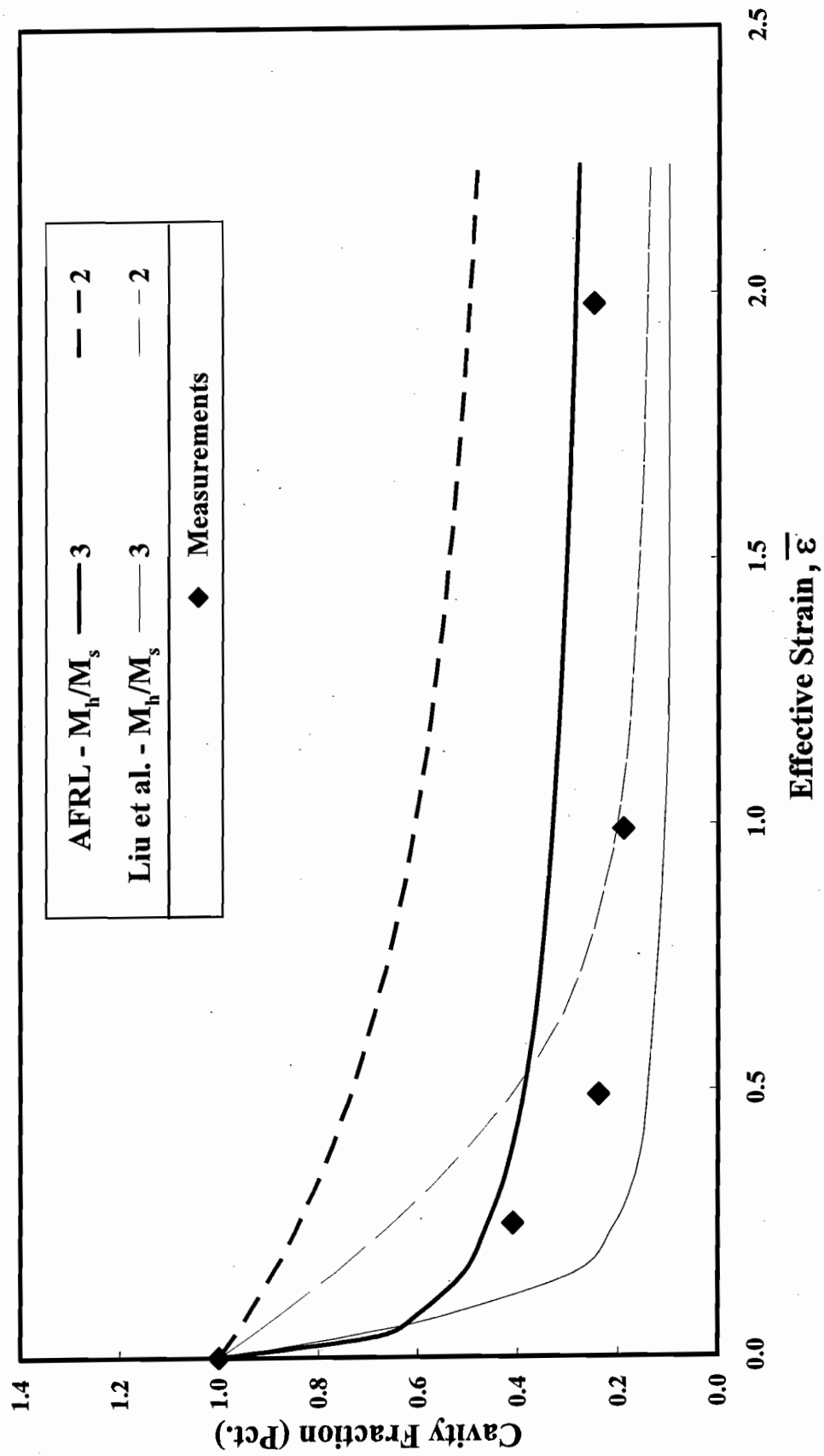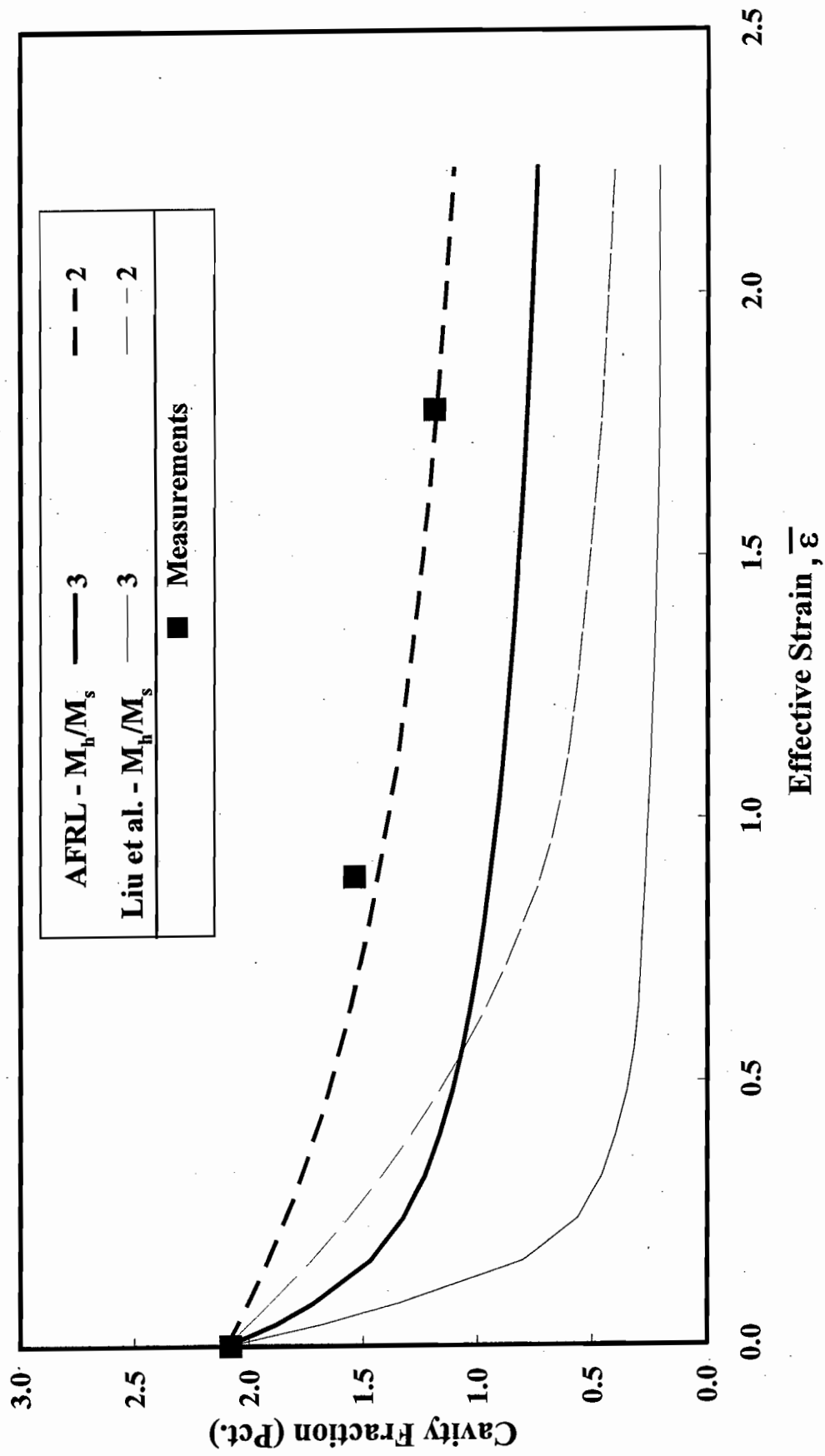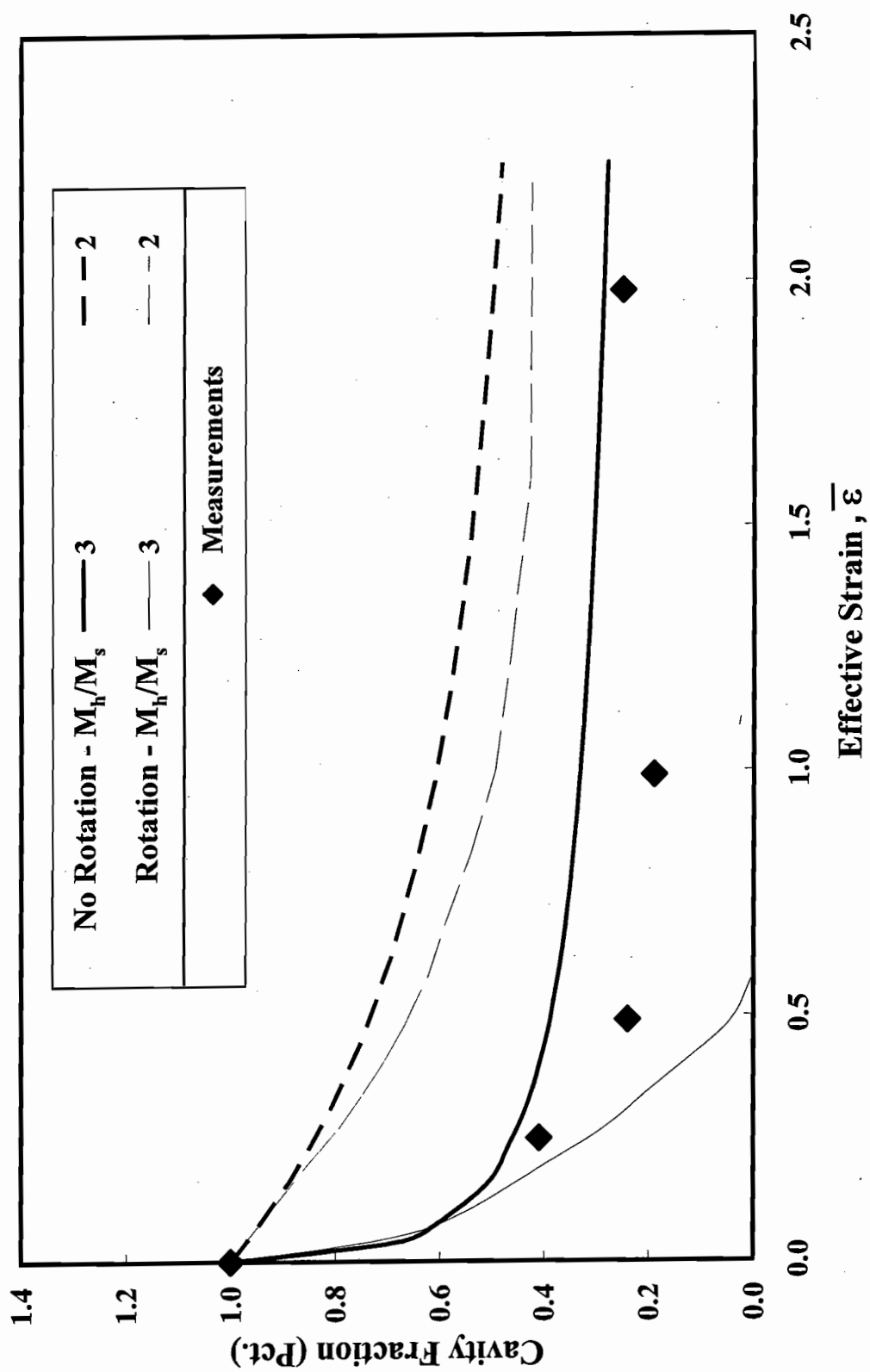
FIGURE 6

20 μm

FIGURE 7

FIGURE 8

29

FIGURE 9

30
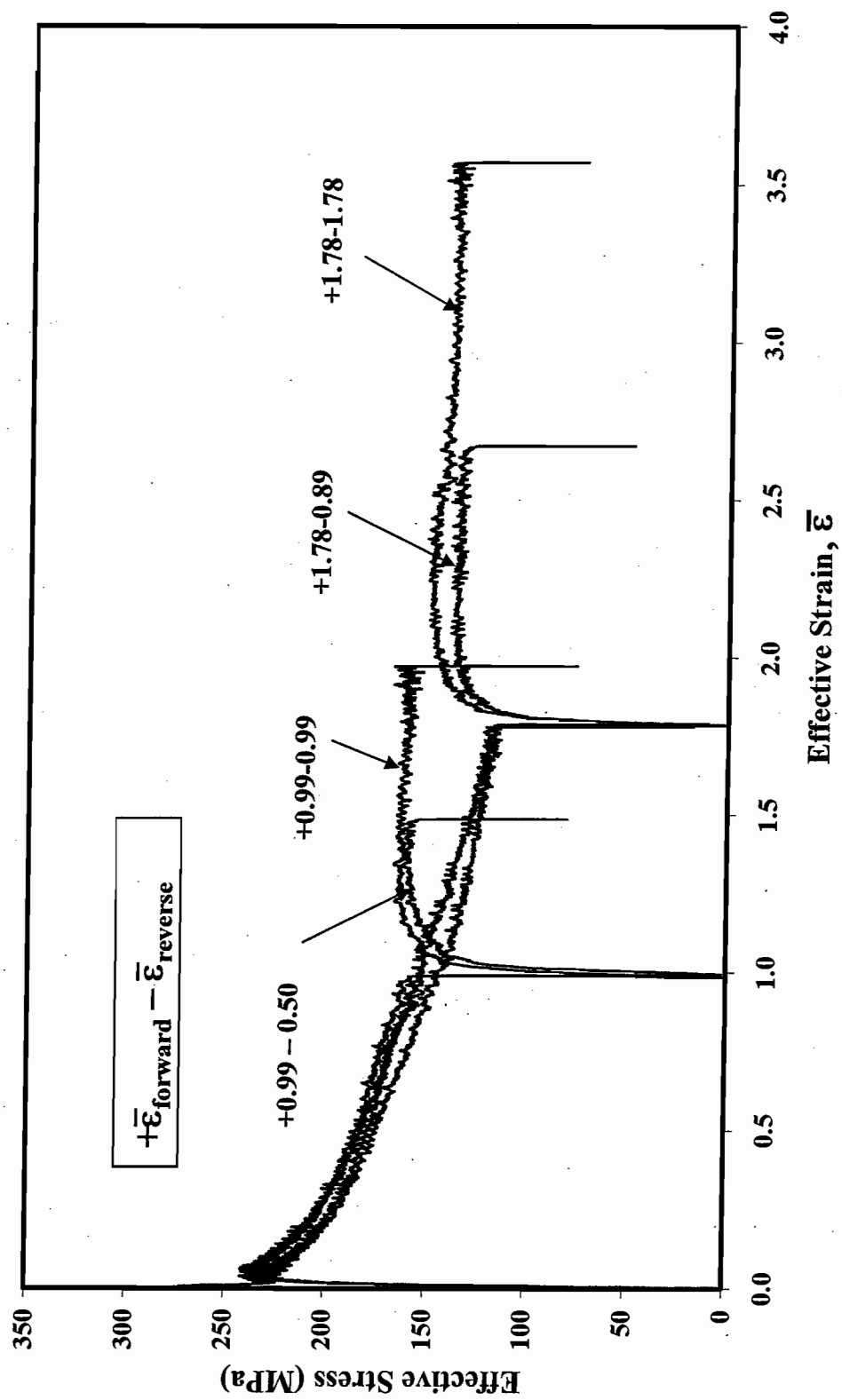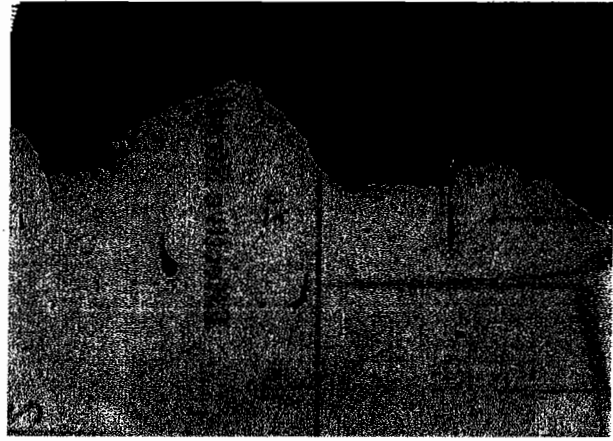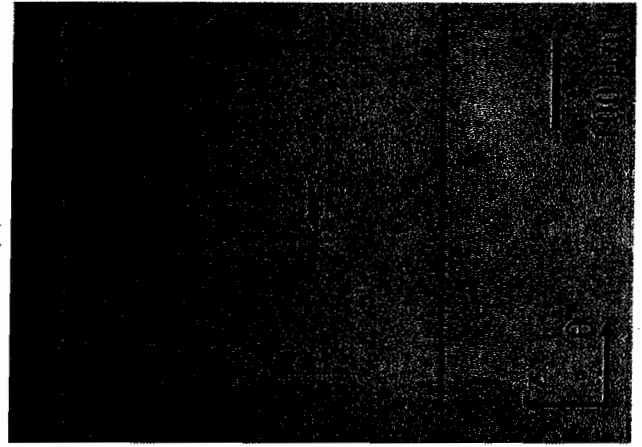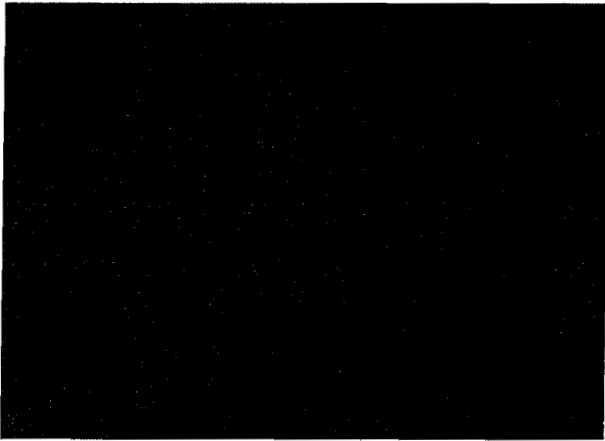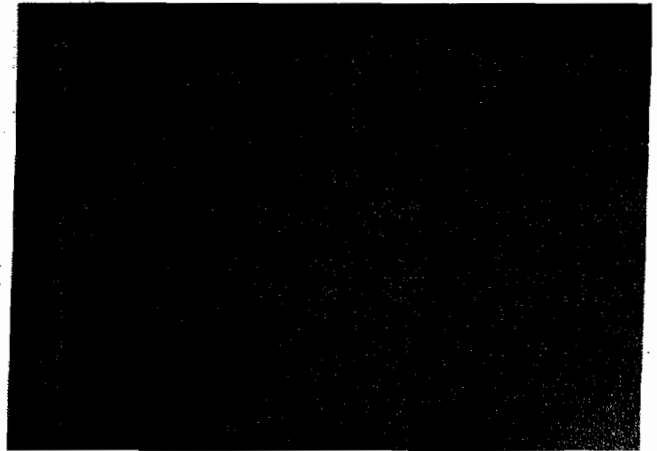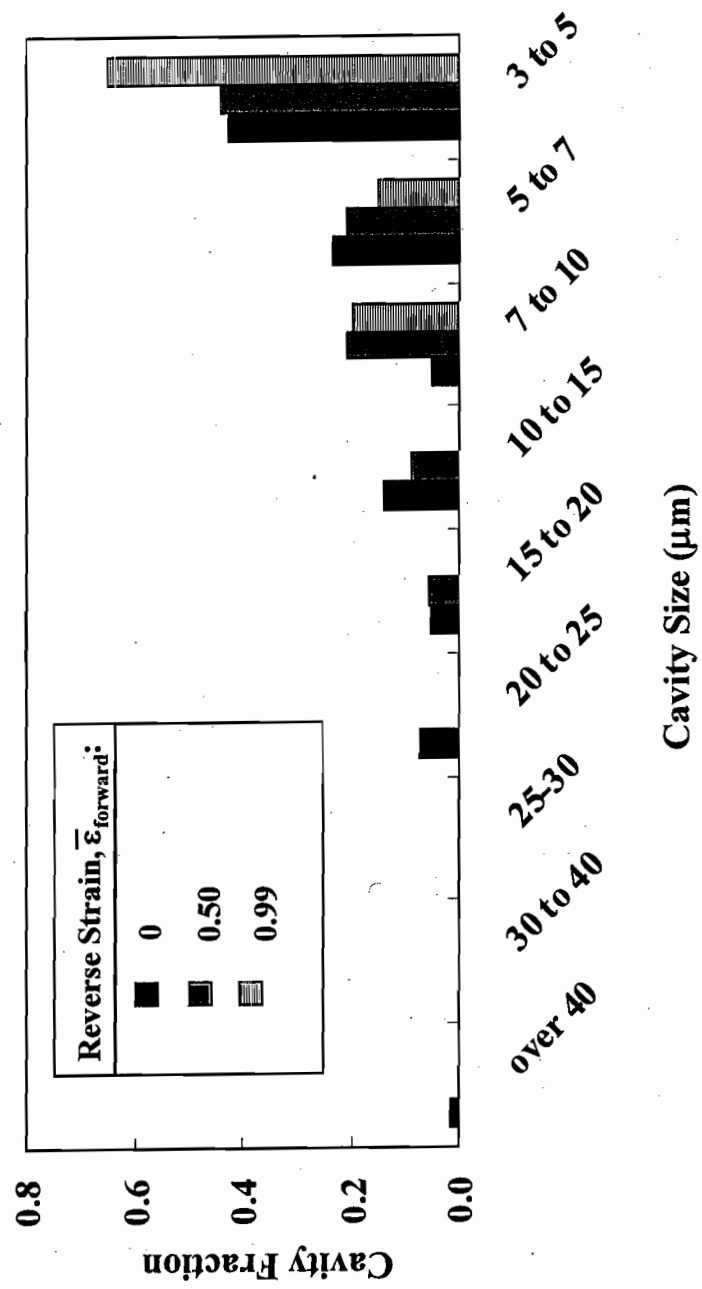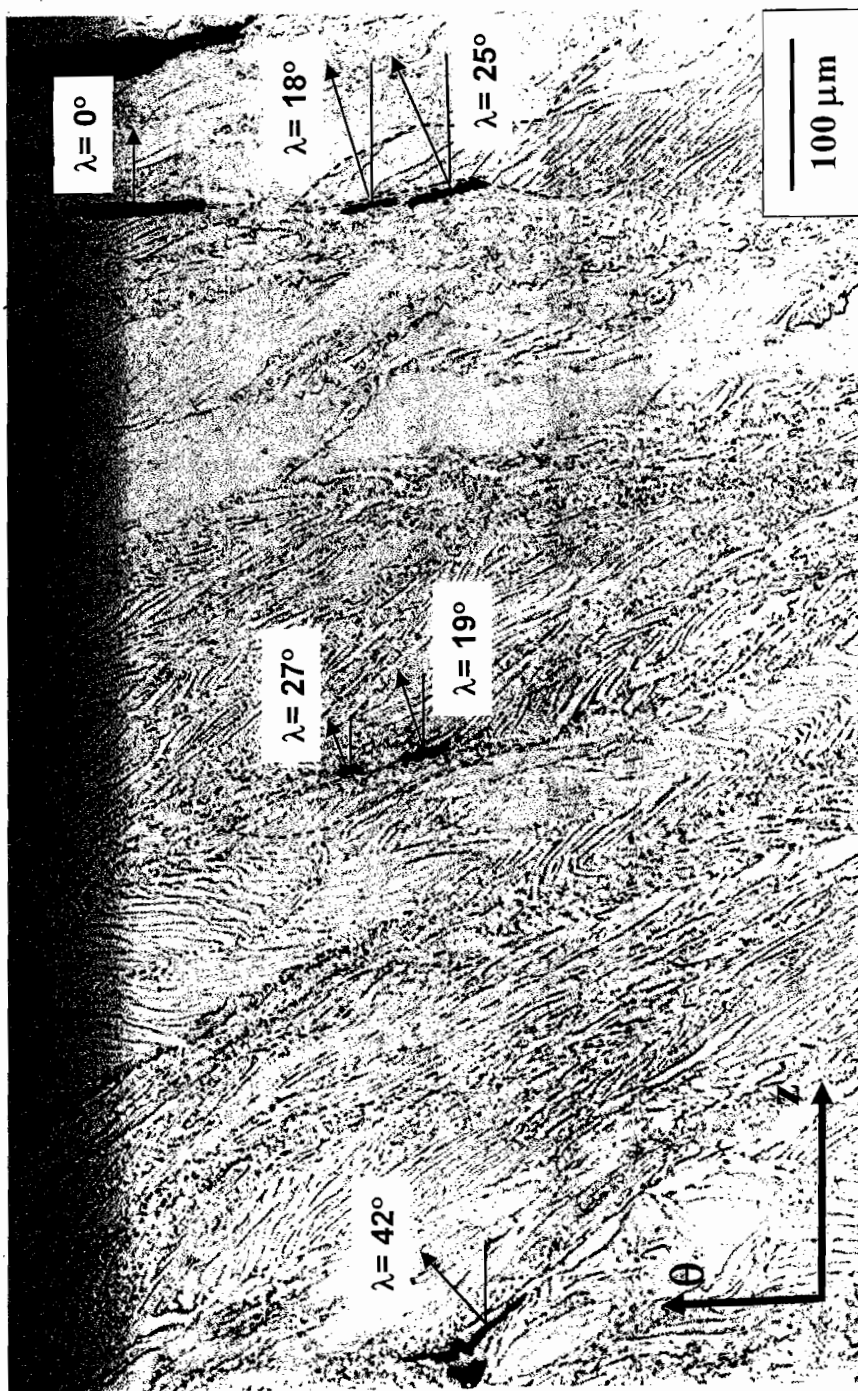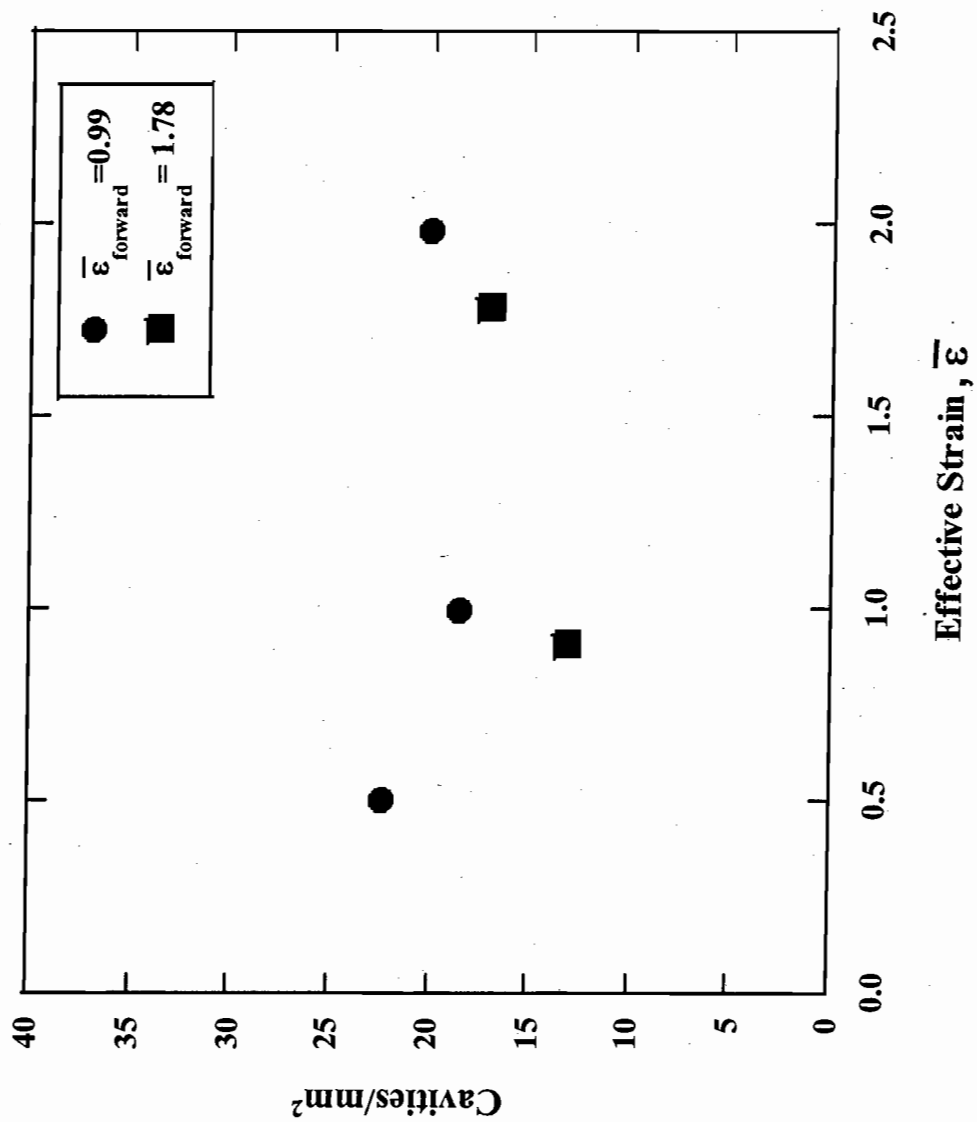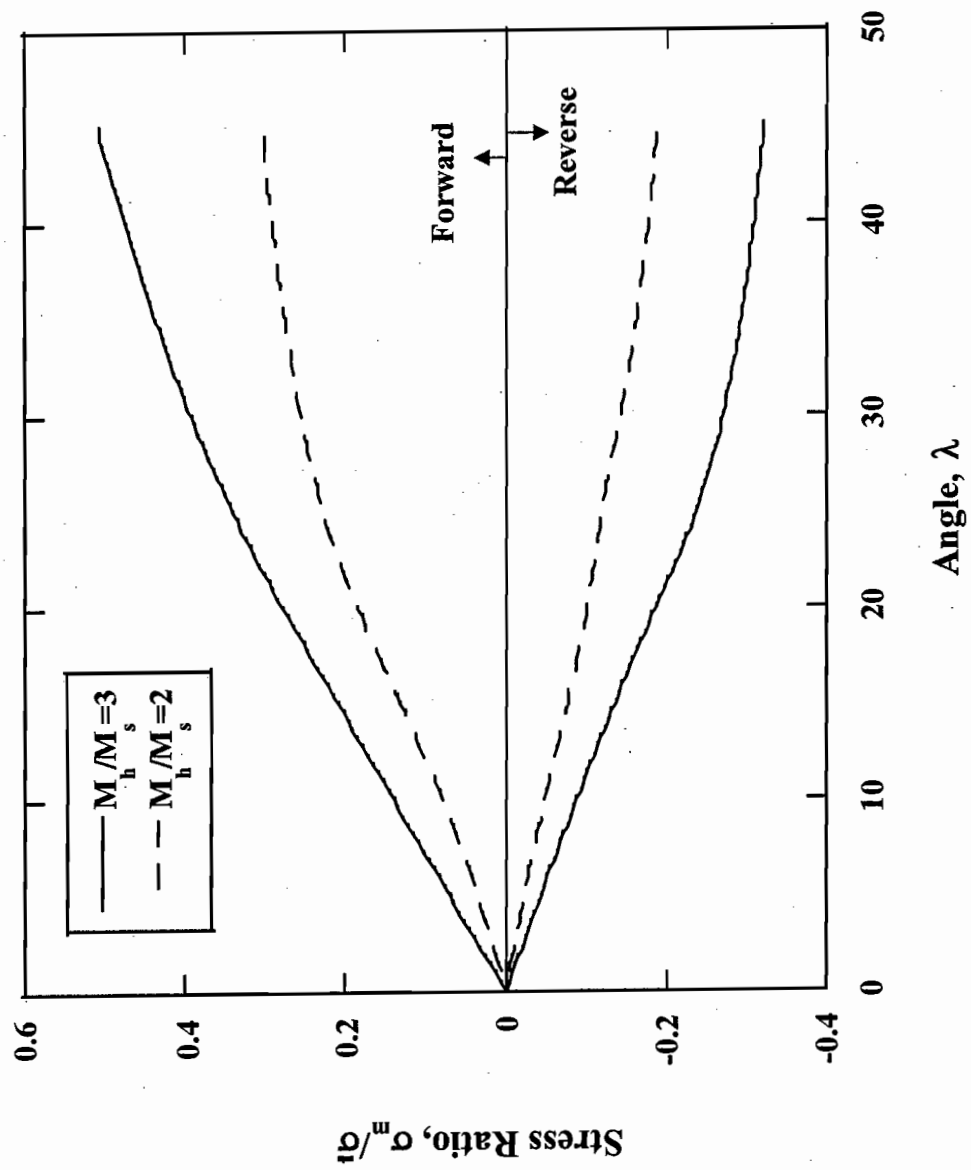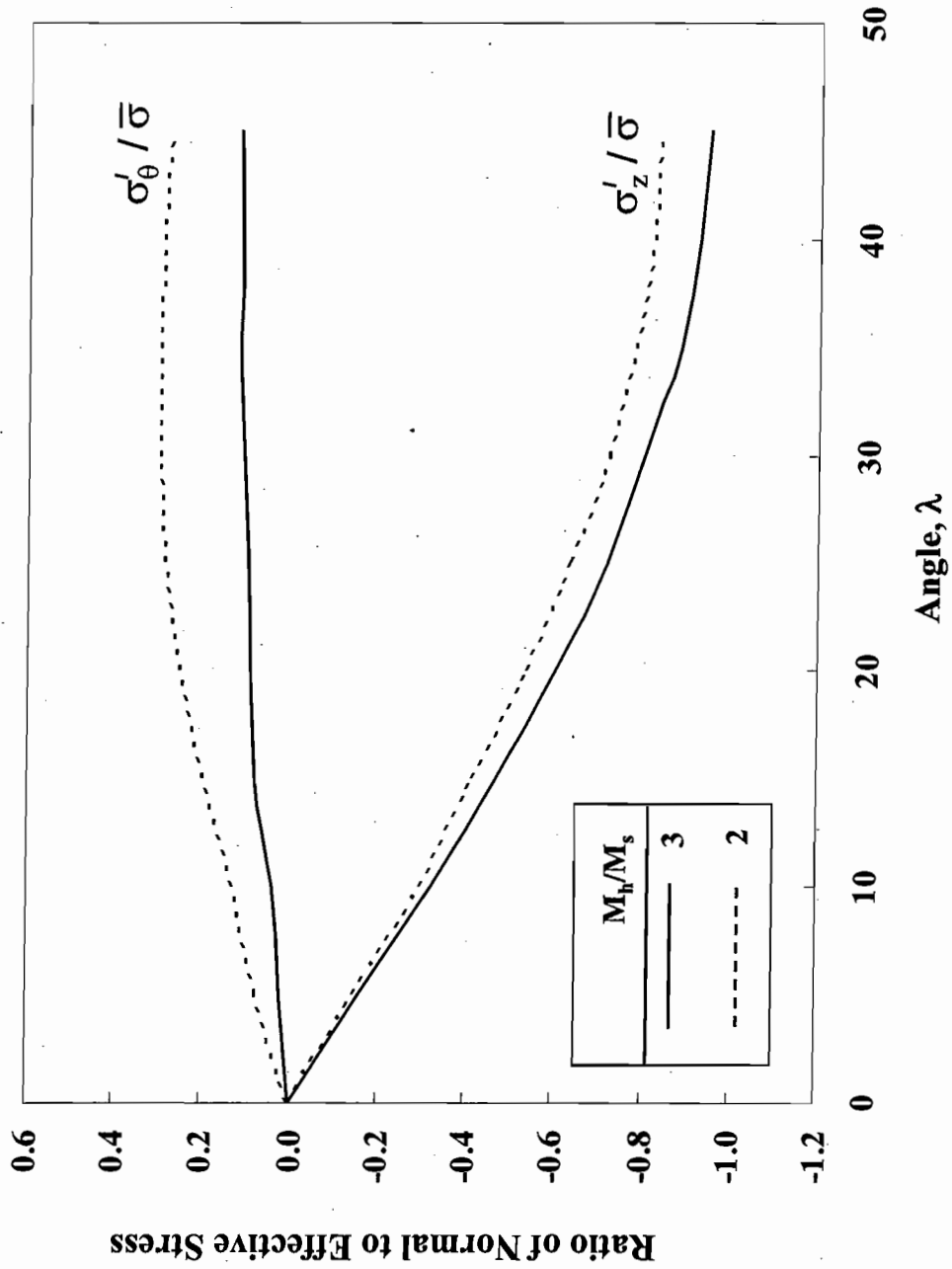
FIGURE 10

FIGURE 11a

32

FIGURE 11b

FIGURE 12a

FIGURE 12b

FIGURE 13